Shape-controlled electrodeposition of tin crystals from Sn(II)-fluoroborate solutions

André Müller*[a], Sara E. C. Dale[a], Miles A. Engbarth[a], Simon J. Bending[a] and Laurence M. Peter[b]

Received (in XXX, XXX) Xth XXXXXXXXX 200X, Accepted Xth XXXXXXXXX 200X

First published on the web Xth XXXXXXXXX 200X

DOI: 10.1039/b000000x

The shape evolution of mesoscopic tin crystals electrodeposited on boron doped diamond (BDD) substrates is described as a function of the ion concentration and deposition potential. Concentrations of 5 – 100 mM Sn(II) in 1 M fluoroboric acid have been explored and electron micrographs of the deposited crystals used to characterise the different shapes and sizes of the crystals obtained. Low concentrations and low overpotentials result in faceted cuboid-shaped crystals while higher concentrations and deposition potentials yield highly complex and fractal-like structures with high surface energies. These crystals can be used as model systems for studying mesoscopic superconductivity, or as a template for core-shell structures if plated with a second metal.

Introduction

The manipulation of the magnetic properties of ferromagnetic and superconducting structures via careful control of their shapes and sizes is currently a topic of major interest worldwide. Bulk β-tin is a type I superconductor below its critical temperature of 3.72 K. A Sn crystal is said to be in the mesoscopic regime when its size is comparable to the temperature-dependent Ginzburg-Landau superconducting coherence length ($\xi(T)\sim 200\ \text{nm} \times (1-T/T_c)^{-1/2}$), at which point its properties will depend intimately on its shape and size. Moreover, the low Ginzburg-Landau parameter, κ, of β-tin and the anisotropy of its superconducting properties along different crystallographic directions[1] make it an ideal material for studying the intermediate state in different confined geometries[2-3]. We demonstrate here that electrodeposition is an excellent approach to fabricate highly faceted three-dimensional (3D) mesoscopic superconducting Sn structures.

Nearly all recent works on mesoscopic superconductivity have used 'top down' nanolithography and etching to pattern two dimensional polycrystalline thin films[4-5]. Electrocrystallisation, in contrast, is capable of readily producing highly faceted 3D single crystal structures with a controllable range of shapes and sizes[6]. This self-assembling route has been thoroughly investigated for a range of practical applications. Tin is widely used in the electronics industry as a coating and soldering material, while tin nanocrystals and nanoneedles have uses as cathodes in microelectronics. Previous work has investigated the deposition of tin films[7] as well as dendritic growth[8-9] and the growth of nanostructures[10-13]. Gómez *et. al.*[14] investigated the nucleation and electrochemical growth of microcrystallites with relatively poorly faceted crystal habits.

Here we report the use of Sn(II) in tetrafluoroboric acid solutions to grow single crystals of tin with typical dimensions of micrometers and a wide variety of shapes. Cuboid-shaped crystals, which are obtained at low overpotentials, represent model systems for probing the superconducting properties of tin in the mesoscopic regime, or as templates for plating with other metals to investigate the interplay of different functional materials in 3D core-shell structures.

Shapes which can be grown from tetrafluoroboric Sn(II) solutions range from simple square cuboids, to highly complex dendritic shapes as tin concentration and growth potential is increased. Polycrystalline boron doped diamond (BDD) as a working electrode has the advantages of a wide potential window, low background currents and chemical inertness. In contrast to highly oriented pyrolytic graphite (HOPG) substrates, diamond can be prepared more uniformly and has a fairly constant low density of nucleation sites associated with the grain boundaries or regions of different local doping densities. Consequently crystals deposited on BDD are well separated.

Experimental

A computer-controlled Potentiostat/Galvanostat (μAutolab type III, Eco Chemie, Utrecht, The Netherlands) was used for these experiments. The electrolyte solutions were freshly prepared from tin(II) tetrafluoroborate solution and Fluoroboric acid solution (both Sigma-Aldrich, U.K.) and Milli-Q water (Millipore, resistivity of 18.2 MΩ cm^{-1}). All solutions were de-aerated with argon before use.

The working electrodes were boron-doped diamonds (BDD) (Windsor Scientific, Berkshire, U.K.) with a boron content of about 0.1 %. The $3\times3\ \text{mm}^2$ diamond substrates were embedded in PTFE to allow easy handling and polished with 3 μm and 1 μm alumina powder (Buhler) on a microcloth (Buehler, Lake Bluff, IL) prior to experiments in order to get a clean surface. After each step the substrates were thouroughly cleaned with DI water. Finally the diamonds were polished using a clean microcloth before cleaning with DI water and blow drying with argon. To avoid any current flow through the corners of the diamond it was masked with a piece of Kapton tape (RS electronics, U.K.) which had a 2.5 mm diameter hole punched through it in the center.

A Ag/AgCl wire was prepared as a reference electrode. A Ag wire (Advent Research Materials Ltd., Oxford, U.K.) was immersed in saturated NaCl solution and a potential of +2 V applied for about 10 s, during which time the wire turned completely black. The same electrode was used as a reference electrode for all experiments. Between experiments the wire

was kept in the dark to avoid degradation. The counter electrode was a platinum foil (Advent Research Materials Ltd., Oxford, U.K.).

Before starting the growth process a potential of +1 V was applied for 30 s to strip off any impurities on the electrode and give it a final clean. This was reduced to 0 V for another 30 s to let the solution and the potentiostat settle, after which a constant overpotential was then applied for a predefined timespan, which was 30 s in most of the experiments. After deposition the diamond was removed from the electrolyte and carefully rinsed with DI water. The DI water was then blown off with a stream of argon, the deposit examined under an optical microscope and imaged with a scanning electron microscope (SEM)(S-4300 Scanning Electron Microscope, Hitachi).

For each investigated solution, a cyclic voltammogram (CV) was made prior to crystal growth with the potential swept at 50 mV/s from +1 V to -1 V.

Due to slightly different doping levels and different surface qualities after each preparation, the working electrodes showed slightly different offsets each time they were used. The potential where the current started to increase, and deposition began, varied by about ±50 mV from run to run and electrode to electrode.

Results and Discussion

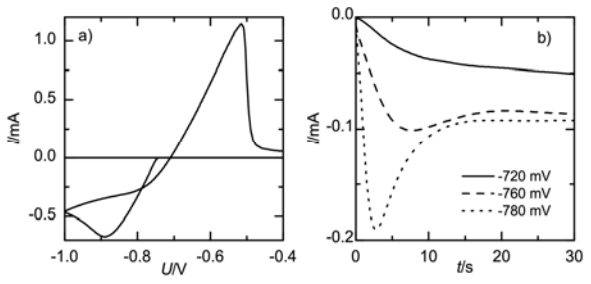

Fig. 1: a) Typical cyclic voltammogram for 25 mM Sn(II) solution with respect to Ag/AgCl reference electrode. Scan rate: 50mV/s. The deposition of tin starts at -710 mV. A reduction peak is visible at -890 mV and an oxidisation peak at -515 mV. b) I-t curve for three different potentials (-720 mV, -760 mV and -780 mV from top to bottom) in 25 mM Sn(II) solution.

In Fig. 1 a) a CV for the 25 mM Sn(II) solution is shown. The CVs for the other solutions are qualitatively similar, although shifted on the potential axis as discussed above and a higher charge transfer is achieved for higher concentrations of Sn(II). For potentials between -0.4 V and +1 V no current flowed. The deposition (abrupt increase of current) started at -710 mV for the 25 mM solution. A reduction peak is visible at -890 mV. For increasing voltages, an oxidation peak is visible at -515 mV. In Fig. 1 b) the current for a constant growth potential is plotted as a function of time. The curves at -720 mV (solid line), -760 mV (dashed line) and -780 mV (dotted line) illustrate the two main regimes which were used to grow the crystals. The lowest overpotential leads to a continuously rising current and hence slow growth of the crystals (kinetically limited growth). The bottom curve at the highest overpotential of -780 mV shows a rapidly increasing current for the first 2.8 s and a decrease thereafter (diffusion

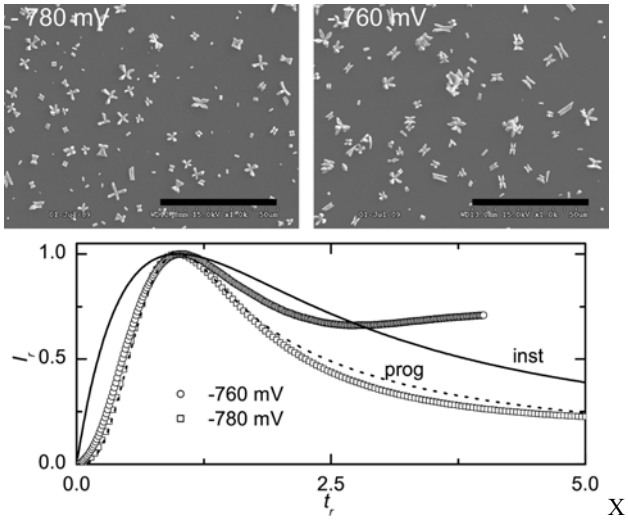

Fig. 2: Electron micrographs of two electrodes at low magnification (scale bar = 50 μm), and the corresponding $I_r = I^2/I_{max}^2$ versus $t_r = t/t_{max}$ plots. Top left:25 mM, -780 mV and top right: 25 mM, -760 mV. The models for instantaneous (upper solid curve) and progressive (lower dotted curve) nucleation after Scharifker and Hills[15] are plotted in the graph for reference.

limited growth). The curve in the middle at -760 mV shows some intermediate behaviour. Our results show that the I-t characteristics of the type shown at low overpotentials lead to the growth of a small number of simple-shaped, faceted crystals such as square cuboids with low surface energies. Higher overpotentials lead to a higher density of crystals and much more complex shapes such as dendrites with very high surface energies. In the following sections a number of different possible crystal habits is described. The focus of attention here is on crystals with sizes greater than a micrometer which are relatively easy to remove from the working electrode and manipulate with a nanopositioner under an optical microsope.

Nucleation

In our system we observe progressive nucleation, according to the model of Scharifker and Hills[15], as can be seen from the I^2/I_{max}^2 versus t/t_{max} graph in Fig. 2. The current transients were analysed for all experiments where the current exhibits a distinct current peak and show the expected behaviour for progressive nucleation mechanism at times shorter than t_{max}. At very low overpotentials, however, the current does not decline at longer times as expected by the S-H model, but persists at a constant, finite value (upper curve at -760 mV in Fig. 2). This indicates that the growth process is not fully diffusion limited as assumed by the S-H model and there is a significant kinetic component[16]. Hydrogen evolution is certainly not responsible for this behaviour since pronounced deviations from the model only occur at low overpotentials.As can be seen from the SEM images in Fig. 2, the crystals on any individual electrode show similar shapes, but differ in size and the stage of their growth. Fig. 2 top shows the nucleation of skeleton-like hollow cuboids at 25 mM and -780 mV and -760 mV respectively.

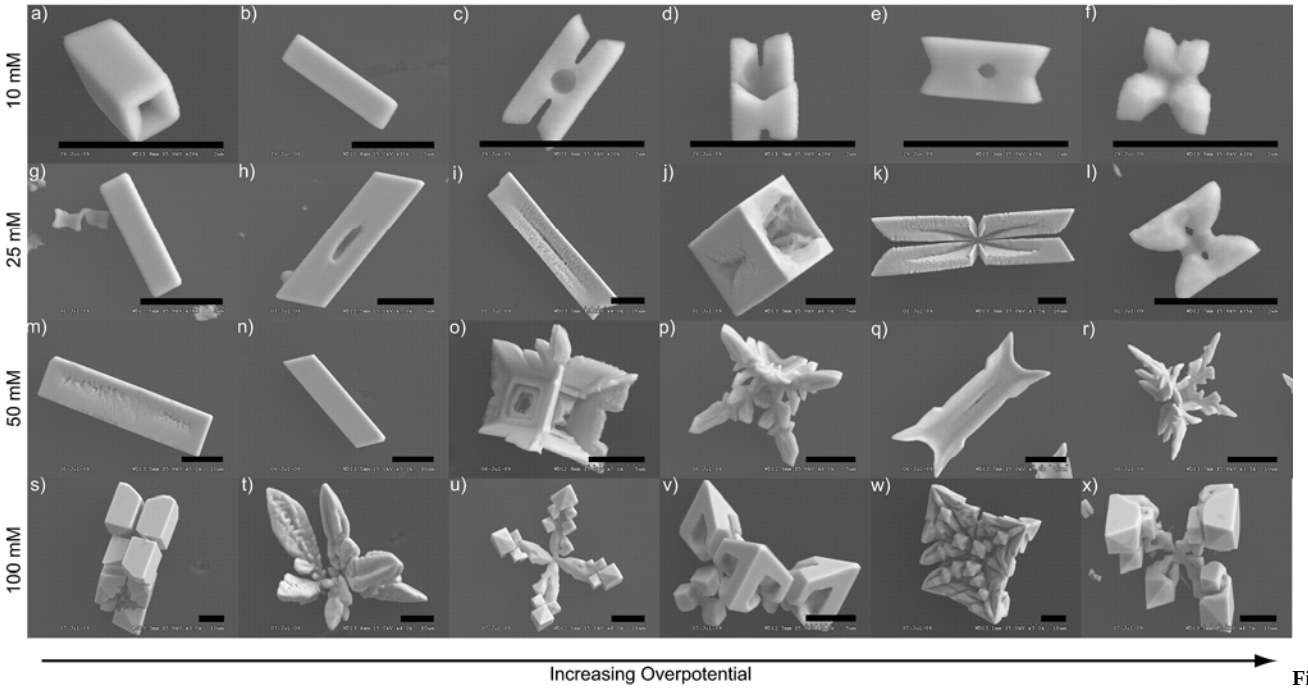

Fig. 3: Electron Micrographs of crystals grown under different conditions. Row one: 10 mM, a) and b) 30 s at -740 mV, c), d) and e) 30 s at -760 mV, f) 30s at -900 mV. Row two: 25 mM, g) and h) 30 s at -720 mV, i) 30 s at -730 mV, j) and k) 90 s at -730 mV and l) 30 s at -780 mV. Row three: 50 mM, m) and n) 30s at -720 mV, o) and p) 30s at -760 mV, q) and r) 30s at -800 mV. Row four: 100 mM, s) and t) 30 s at -800 mV, u) and v) 30 s at -820 mV, w) 30 s at -860 mV and x) 30 s at -900 mV. The scale bar is 5 μm in all cases

Mechanism of tin Growth

Tin crystals grow on BDD electrodes according to the Volmer-Weber mechanism, as it is more favourable for Sn(II) ions to bind with already nucleated tin atoms, than to start growing a new nucleus. The growth mechanism of tin dendrites from $SnCl_2$ in HCl was described by G. Wranglén[8] and can be adopted to inform our understanding of the orientation and growth of the microcrystals prepared in our experiments. Individual crystals have been manipulated on the growth electrode in order to fully characterise their 3D geometries. In this way the different sizes, orientations and development of single crystals enables an overview of the growth process to be obtained. β-Sn crystallises in a body-centred tetragonal lattice with a two atom basis and a = b = 5.82 Å and c = 3.17 Å. The two atoms of the basis are ½ a and ¼ c apart. The dendrites grown by Wranglén grew along the [110] direction and consisted of single pyramids with the tip pointing in the [001] direction. The theoretical angle between the (001) plane (base of the pyramid) and the (101) plane (side of the pyramid) is 28.6°. The low cohesion energy of tin[14] facilitates the development of highly faceted crystals for low depostion potentials. Very slow growth allows atoms plenty of time to diffuse at crystal surfaces and realise the lowest surface energy structures. Although our structures do not show a sequence of pyramids, similar geometric considerations appear to govern the typical structures that we observe. The evolution of crystal habits as a function of deposition conditions is shown in Fig. 3. In general an increase in complexity and size is visible for higher concentrations, especially at high overpotentials. The first row of images shows crystals that were grown from 10 mM Sn(II). (a and b) show relatively large square cuboid rods, while the crystal in a) seems to be hollow. For higher potentials, (c - f), the crystals look like the outer skeleton of a square cuboid with defects along the middle and in the centre. The crystals grown from a 25 mM solution are larger for the same growth time, but still show a general cuboid shape. Low

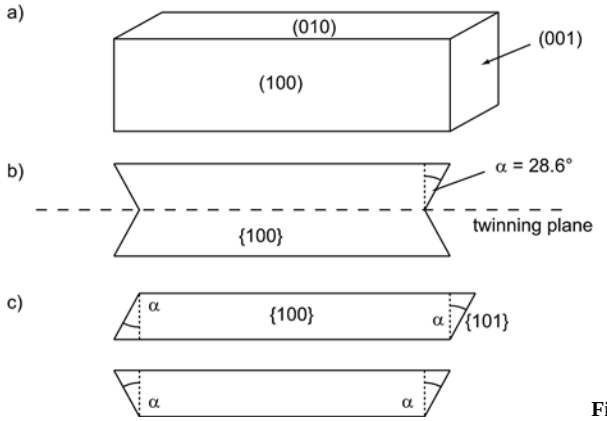

Fig. 4: The crystallographic orientation of some of the structures observed. a) the general growth planes and directions, b) symmetric growth about a twinning plane, c) asymmetric growth.

overpotentials, (g - i), lead to ordered square cuboid crystals, while higher overpotentials and longer growth times, (j - l), yield mostly hollow skeletons with an exterior cuboid shape. The two bottom rows show crystals from the highest

investigated concentrations. Low overpotentials still lead to rather complete, solid square cuboids (m) while higher overpotentials lead to very complex, dendritic crystals, (o - r and t - x). There are, however, still cuboid structures visible in the crystals. For example in Fig. 3 (u and w) the crystal 'scaffold' looks like a number of cuboids held together by an outer skeleton. The pyramid angle described above can be seen in many of our crystals e.g. in Fig. 3 (c, e, h and k). Here the end of the cuboid is cut at exactly this angle (cf., Fig. 4(b)), while for Fig 3 (h and n) the end is cut at an angle of about 30° (cf., Fig. 4(c)). For the crystals in Fig. 3 (c, e and k) the cavity is symmetric around the center of the crystals, suggesting that a twin plane runs through the crystal. These observations indicate that the long axis of the cuboids corresponds to the [001] direction, while the two (equal) short lengths are along the two equivalent directions [100] and [010] (cf. Fig. 4(a)), consistent with the conclusions of ref.[14]. This is the shape expected for a slow kinetically-limited growth when the energetically-favoured high atomic density surfaces are selected.

For higher concentrations and overpotentials the growth mechanism changes. The fastest growth seems to happen along the body diagonal [111] direction (e.g. Fig. 3 (o and p)) while the faces of the cuboid are only partially developed. For the highest concentration (Fig. 3 bottom row) the crystals grow in a dendritic, fern-like manner. The crystals in Figs. 3(u and x) show, in particular, that the structures still grow as

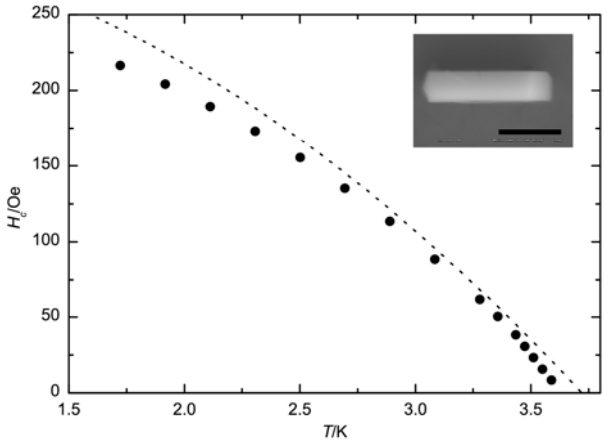

Fig. 5: The critical magnetic field of a $4.8 \times 1.2 \times 1.2$ μm^3 square cuboid tin sample with a pyramidal end cap as a function of temperature (circles) and the same dependence for bulk tin[17] (dotted line). The inset shows an SEM image of the sample.

single crystals, albeit multiply-twinned ones. The main branches are of quite irregular shapes but at the end caps the cuboid parts are arranged along identical axes. Spherical diffusion layers are formed around more acute pointed parts of the crystal, resulting in more efficient 3D diffusion. This leads to faster growth at these locations and incident atoms have little time to diffuse on the surface, resulting in a highly non-equilibrium surface structure. This explains the formation of the skeletons, since the fastest growth occurs at the corners rather than the faces of the crystal. This is also the origin of the dendritic growth when, even further away from equilibrium, the crystal grows preferentially at the crystal corners rather than at edges or on faces[9].

The superconducting properties of many of the crystal types shown in Fig. 5 have been characterised by Hall probe array micromagnetometry[5]. All samples tested have been superconducting with a critical temperature very close to the value of 3.72 K characteristic for high quality bulk samples.

Fig. 5 shows a plot of the temperature dependent critical field for a relative large, electrodeposited square cuboid sample with dimensions $4.8 \times 1.2 \times 1.2$ μm^3 (Fig. 5 inset). This is in good agreement with the expected form of $H_c(T)$[17] for bulk tin which is also indicated. A detailed study of the superconducting properties of Sn microcrystals of different sizes and shapes will be reported elsewhere.

Conclusion

Our results clearly demonstrate that the deposition of tin from fluoroboric acidic solutions yields a large variety of crystal shapes and sizes. While the deposition of simple square cuboid shaped crystals dominates over a range of different concentrations for low applied overpotentials, higher overpotentials result in highly complex crystals, whose shape is increasingly complicated for higher concentrations. Nevertheless these samples appear to be single crystals, or multiply-twinned single crystals, as determined from an analysis of their shapes. The ready availability of the electrolyte materials and the ease with which crystals of different sizes and shapes can be realised makes this a powerful and versatile approach for preparing mesoscopic Sn samples with micrometer dimensions.

Acknowledgments

This work was supported by the Engineering and Physical Sciences Research Council (EPSRC) in the U.K. under grant number EP/E039944/1.

Notes and references

[a] *Department of Physics, University of Bath, Bath BA2 7AY, UK; E-mail: A.Mueller@Bath.ac.uk*
[b] *Department of Chemistry, University of Bath, Bath BA2 7AY, UK*

1. P. C. L. Tai, M. R. Beasley and M. Tinkham, *Phys. Rev. B: Solid State*, 1975, **11**, 411.
2. R. N. Goren and M. Tinkham, *J. Low Temp. Phys.*, 1971, **5**, 465.
3. V. A. Schweigert and F. M. Peeters, *Phys. Rev. B: Condens. Matter*, 1999, **60**, 3084.
4. V. V. Moshchalkov, L. Gielen, C. Strunk, R. Jonckheere, X. Qiu, C. V. Haesendonck and Y. Bruynseraede, *Nature*, 1995, **373**, 319.
5. A. K. Geim, I. V. Grigorieva, S. V. Dubonos, J. G. S. Lok, J. C. Maan, A. E. Filippov and F. M. Peeters, *Nature*, 1997, **390**, 259.
6. Z.-L. Xiao, C. Y. Han, W.-K. Kwok, H.-H. Wang, U. Welp, J. Wang and G. W. Crabtree, *J. Am. Chem. Soc.*, 2004, **126**, 2316.
7. M. C. Santos and L. O. S. Bulhões, *Electrochim. Acta*, 2003, **48**, 2607.
8. G. Wranglén, *Electrochim. Acta*, 1960, **2**, 130.
9. K. Fukami, S. Nakanishi, H. Yamasaki, T. Tada, K. Sonoda, N. Kamikawa, N. Tsuji, H. Sakaguchi and Y. Nakato, *J. Phys. Chem. C*, 2007, **111**, 1150.
10. N. H. Chou and R. E. Schaak, *Chem. Mater.*, 2008, **20**, 2081.
11. C. Lizzul Rinne, J. J. Hren and P. S. Fedkiw, *J. Electrochem. Soc.*, 2002, **149**, C150.

12. M. Tian, J. Wang, J. Snyder, J. Kurtz, Y. Liu, P. Schiffer, T. E. Mallouk and M. H. W. Chan, *Appl. Phys. Lett.*, 2003, **83**, 1620.
13. J. Torrent-Burgués, E. Guaus and F. Sanz, *J. Appl. Electrochem.*, 2002, **32**, 225.
14. E. Gómez, E. Guaus, F. Sanz and E. Vallés, *J. Electroanal. Chem.*, 1999, **465**, 63.
15. B. Scharifker and G. Hills, *Electrochim. Acta*, 1983, **28**, 879.
16. G. Oskam, P. M. Vereecken and P. C. Searson, *Journal of The Electrochemical Society*, 1999, **146**, 1436-1441.
17. J. Feder and D. S. McLachlan, *Phys. Rev.*, 1969, **177**, 763.